

# In-Beam PET And Compton Imaging For Enhanced Accuracy Proton-Range Verification

**Javier Balibrea-Correa** (✉ [javier.balibrea@ific.uv.es](mailto:javier.balibrea@ific.uv.es))

Instituto de Física Corpuscular, CSIC-University of Valencia

**Jorge Lerendegui-Marco**

Instituto de Física Corpuscular, CSIC-University of Valencia

**Ion Ladarescu**

Instituto de Física Corpuscular, CSIC-University of Valencia

**César Domingo-Pardo**

Instituto de Física Corpuscular, CSIC-University of Valencia

**Carlos Guerrero**

Universidad de Sevilla

**Teresa Rodríguez-González**

Universidad de Sevilla

**Maria del Carmen Jiménez-Ramos**

Centro Nacional de Aceleradores (Universidad de Sevilla-Junta de Andalucía-CSIC)

**Begoña Fernández-Martínez**

Universidad de Sevilla

---

## Research Article

### Keywords:

**Posted Date:** March 7th, 2022

**DOI:** <https://doi.org/10.21203/rs.3.rs-1360878/v1>

**License:**  This work is licensed under a Creative Commons Attribution 4.0 International License.

[Read Full License](#)

---

# In-beam PET and Compton imaging for enhanced accuracy proton-range verification

Javier Balibrea-Correa<sup>1,\*</sup>, Jorge Lerendegui-Marco<sup>1</sup>, Ion Ladarescu<sup>1</sup>, César Domingo-Pardo<sup>1</sup>, Carlos Guerrero<sup>2</sup>, Teresa Rodríguez-González<sup>2,3</sup>, Maria del Carmen Jiménez-Ramos<sup>3,4</sup>, and Begoña Fernández-Martínez<sup>2,3</sup>

<sup>1</sup>Instituto de Física Corpuscular, CSIC-University of Valencia, Valencia, Spain

<sup>2</sup>Dept. de Física Atómica, Molecular y Nuclear. Universidad de Sevilla, Seville, Spain.

<sup>3</sup>Centro Nacional de Aceleradores (Universidad de Sevilla-Junta de Andalucía-CSIC), Seville, 41092, Spain

<sup>4</sup>Department of Applied Physics II, ETSA, University of Seville, Seville, Spain

\*javier.balibrea@ific.uv.es

## ABSTRACT

We report on a combined in-beam PET and prompt-gamma Compton imaging system aimed at ion-range verification in proton-therapy treatments. A proof-of-concept experiment was carried out at the radiobiology beam line of the CNA cyclotron facility using a set of two synchronous Compton imagers and different target materials. The time structure of the 18 MeV proton beam was shaped with a series of beam-on and beam-off intervals, thereby mimicking a pulsed proton beam on a long time scale. During beam-on Compton imaging was performed utilizing the high energy  $\gamma$ -rays promptly emitted from the nuclear reactions in the target. In the course of the beam-off intervals in-situ positron-emission tomography was accomplished with the same imagers using the  $\beta^+$  decay of short-lived activated nuclei. The targets used were stacks of different materials covering also various proton ranges and energies. The experimental results obtained in this work are compared with a Monte Carlo model of the experimental setup. The results demonstrate the possibility to combine both imaging techniques in a concomitant way, where high-efficiency Compton imaging is complemented with the high spatial accuracy of PET. Empowered by these results we discuss a new methodology for enhanced accuracy and real-time ion-range monitoring. We suggest that a pulsed beam with a suitable duty cycle, in conjunction with in-situ Compton- and PET-imaging may help to attain both real-time and high-accuracy range monitoring.

## Introduction

Accurate ion-range determination is a key aspect in modern proton-therapy treatments<sup>1</sup>. This technique allows one to target very precisely the tumor area thanks to the large energy deposition at the end of the proton track (Bragg peak). As a consequence, hadron therapy minimizes damage in neighbouring tissues, thereby reducing also long term secondary effects. Hence, it is particularly well-suited for many pediatric cases and tumors close to sensitive organs<sup>1</sup>. However, the full potential of proton therapy is still hindered by the lack of high-accuracy real-time range verification, which would enable to use particle beams as a precise and non-invasive scalpel. This could extend the applicability of proton therapy also to diseases such as ventricular tachycardia and many other cardiovascular disorders<sup>2-4</sup>, thereby enlarging the number of patients benefiting from therapeutic high-energy beams.

As the incident proton beam slows down and stops inside the patient tissue, nuclear reactions take place all along the projectile path producing quasi-instantaneously (prompt) emission of secondary radiation<sup>5</sup>. This radiation, mainly  $\gamma$ -rays with energies spanning up to 5-6 MeV, are especially well suited to monitor the range of the ion beam. Prompt-Gamma (PG) monitoring has the advantage of the high spatial correlation with the primary ion range<sup>5</sup>. From a practical point of view, a major challenging aspect for real-time PG monitoring is the small signal-to-background ratio, which is commonly constrained by the limited efficiency of the detection apparatus, by the contaminant radiation arising from proton-beam interactions along different parts of the accelerator gantry, as well as by neutron contaminant reactions in the measuring instruments and in different parts of the surrounding area<sup>1,6</sup>.

In addition to PG monitoring there are other detection techniques for ion range verification, such as in-beam and off-beam PET imaging<sup>1,7</sup>. The latter is obviously not suited for real-time range assessment and in this work we discuss only the former. This methodology is based on the simultaneous detection of two 511 keV annihilation  $\gamma$ -rays coming from the  $\beta^+$  decay of short-lived nuclei activated by the hadron beam. The most abundant  $\beta^+$  emitters produced during the treatment are <sup>15</sup>O and <sup>11</sup>C with half-lives of 112 s and 20.4 m, respectively. The latter are mainly suited for a PET imaging control only after irradiation<sup>8-10</sup>.

35 Several configurations have been proposed for in-beam PET imaging starting from the simplest two detection systems working  
36 in time-coincidence to complex cylindrical ring configurations<sup>11,12</sup>. The latter have evolved toward a combination of PET and  
37 Compton imaging<sup>13,14</sup>, similar to the approach discussed in this work, but aimed at other clinical applications.

38 Our detection system is based on modular and high-efficiency Compton cameras, called i-TED<sup>15</sup>. The latter have been  
39 specifically designed for neutron-capture nuclear physics experiments using the Time-Of-Flight (TOF) technique<sup>16,17</sup>. In  
40 this type of experiments, the  $\gamma$ -ray yields from the  $(n, \gamma)$  reactions of interest are rather weak compared to the background  
41 arising from contaminant neutron interactions in different materials of the experimental area. Also, neutron capture  $\gamma$ -ray  
42 energies of interest typically span from hundreds of keV up to 5-6 MeV. Developments made to optimize the last two aspects in  
43 nuclear-physics experiments are also well suited for the implementation of i-TED in the present application. Thus, each i-TED  
44 module consists of two planes of Position Sensitive Detectors (PSD) and, aiming at maximizing detection efficiency, each PSD  
45 uses largest commercially available  $\text{LaCl}_3(\text{Ce})$  monolithic scintillation crystals with a size of  $50 \times 50 \text{ mm}^2$  optically coupled to  
46  $8 \times 8$  pixels Silicon Photomultipliers (SensL ArrayJ-60035-65P-PCB). To enhance further the solid angle for Compton events  
47 each absorber plane consists of four, 25 mm thick, PSDs covering an area of  $100 \times 100 \text{ mm}^2$  in each i-TED module. For a  
48 point-like 1 MeV  $\gamma$ -ray source at 5 cm distance from the front face of the module, the coincidence detection efficiency is  
49  $\sim 0.2\%$ . Regarding neutron-induced background suppression,  $\text{LaCl}_3(\text{Ce})$  ensures a small sensitivity to neutron interactions  
50 in the detection volume itself<sup>18</sup>, while offering also a large intrinsic detection efficiency. Finally, the high time-resolution  
51 obtained with the implemented acquisition system (PETsys Front-End Board D version 2 (FEB/D-1024)), with coincidence-time  
52 resolutions of  $\text{CTR} \sim 500 \text{ ps}$ , help to reduce random coincidences and other related backgrounds that could degrade the Compton  
53 imaging. For further details of the i-TED modules and developments on the  $\gamma$ -ray position reconstruction the reader is referred  
54 to<sup>15,19</sup>.

55 In this work we explore the applicability and performance of two i-TED modules working independently as PG Compton  
56 and in-beam PET imagers, using different time-coincidence strategies between the PSDs of the i-TED modules and a pulsed  
57 beam-time structure. A study of the performance of i-TED as Compton- and PET-imager is reported below in Methods, in  
58 section Laboratory characterization of the i-TED imaging system. The combined PG monitoring and in-beam PET experiment  
59 was carried out at the radiobiology beam line of the 18 MeV proton cyclotron facility at CNA<sup>20</sup> during two consecutive days.  
60 Radiobiological research using this type of low energy particle accelerators has attracted a lot of interest in the last decades  
61 concurring with the worldwide expansion of hadron-therapy centers<sup>21</sup>.

62 The cyclotron facility at CNA consists of a Cyclone 18/9 model equipped with an external beam line for multi-purpose  
63 research. The cyclotron accelerates protons and deuterons to 18 and 9 MeV, respectively. The beam is then delivered to the  
64 dedicated experimental area through a complex beam extraction system. For further details about the research beam line the  
65 reader is referred to<sup>22</sup>.

66 During the experiment, a 18 MeV proton beam was delivered to the experimental area with current values varying from 500  
67 pA up to 1 nA on target, adding-up a total charge ranging from 212 to 674 nC per irradiation, depending on the total irradiation  
68 time and specific duty cycle used that will be explained later.

69 A picture of the experimental setup is displayed in Fig. 1. This configuration was chosen for a twofold study, on the one  
70 hand, to measure proton-induced  $\beta^+$ -emitter production cross sections<sup>23</sup> and, on the other hand, to explore the combination of  
71 Compton and PET imaging for ion-range verification, which is the main objective of this article. The proton beam direction  
72 is indicated by the red arrow. A sample holder (elongated U-shaped piece in the center) was used to simultaneously expose  
73 regularly spaced thin sample-foils to the proton-beam. Both the holder and the samples themselves were specifically designed  
74 for a parallel study devoted to the determination of production cross sections of  $\beta^+$  emitting isotopes<sup>23,24</sup>. However, as  
75 discussed later, this set-up turned out to be very well suited for the simultaneous demonstration of PET and Compton imaging  
76 discussed in this work. The holder was aligned with the proton beam axis, thereby inducing a similar irradiation field for all  
77 samples under study. The material of the samples holder was polylactic acid (PLA) plastic with a size of  $5.2 \times 5.5 \times 10.3 \text{ cm}^3$ .  
78 The central hole had a size of  $3.2 \times 4.12 \text{ cm}^2$ . The target samples consisted of thin layers of different materials (described  
79 below), which were placed using five dedicated slots with a regular gap of 1.6 cm. The samples consisted of thin square layers  
80 with dimensions of  $41.2 \times 41.2 \times 0.8 \text{ mm}^3$ , fitting into the dedicated slots of the holder. Two different materials were used, Nylon  
81 and PMMA, with nominal densities of 1.15 and 1.18  $\text{g/cm}^3$ , respectively. At the very end of the samples holder a 2 mm thick  
82 graphite layer was added, with the twofold purpose of fully stopping the proton beam and registering the proton-current values  
83 during the experiment.

84 The holder-samples assembly was supplemented with an additional PLA matrix, which is also shown in Fig 1. This PLA  
85 matrix was remotely controlled and designed to fill the gap between the samples after each proton-beam irradiation, thereby  
86 acting as  $\beta^+$  converter and lowering the spatial range of the  $\beta^+$  particles when inserted. Fig. 2 shows a schematic drawing of  
87 the moderator-converter assembly, which can help to get a better understanding of this set-up.

88 The two i-TED modules used during the experiment were placed front-to-front on both sides of the proton beam axis, fully  
89 covering the in-beam PET field of view of the samples under study. The i-TED module labelled as i-TED-A used an aluminum

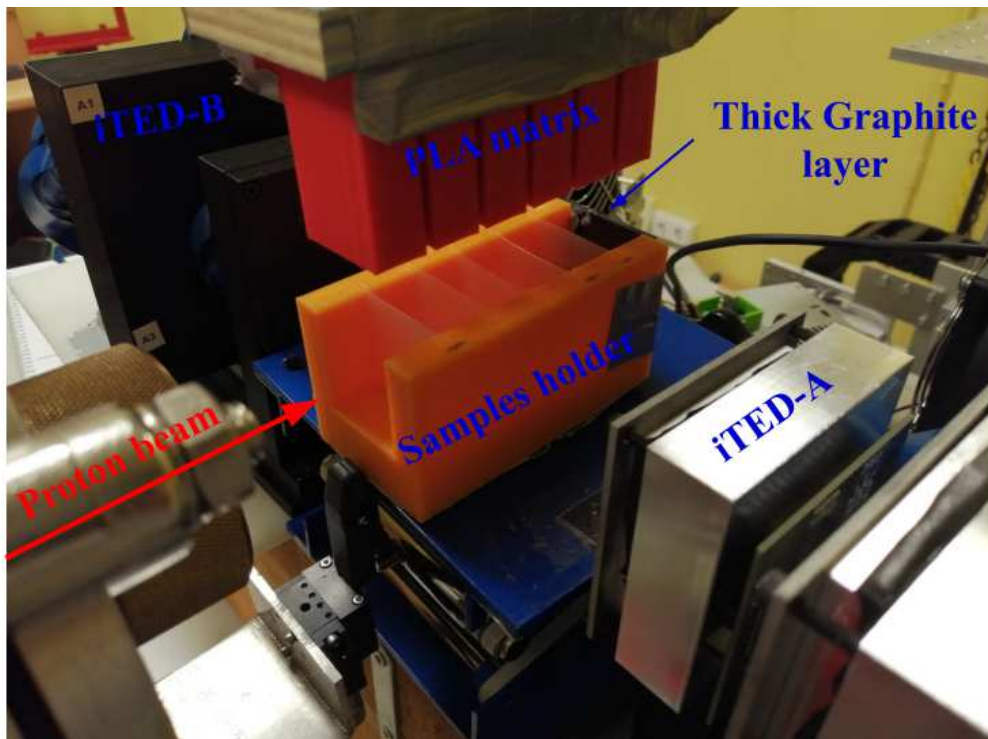


**Figure 1.** Experimental setup used during the proof-of concept experiment. At both sides of the samples two i-TED modules were set-up. See text for details.

90 housing and was placed at 5.9 cm from the sample holder. The second one, labelled as i-TED-B and encapsulated in black PLA  
 91 housing, was situated at 5.1 cm from the samples holder as shown in Fig. 1. The distance between the front face of the scatter  
 92 plane of both i-TED modules was 27.5 cm. Owing to the primary goal of the experiment, which was the measurement of  $\beta^+$   
 93 emitters, the distance between detection planes in each i-TED module was set to the minimum possible (2.6 cm) in favor of  
 94 increasing the in-beam PET efficiency at the cost of worsening the angular resolution of the Compton images reconstructed  
 95 from the individual i-TED modules<sup>15</sup>.

96 The 10 PSDs embedded in both i-TED modules comprised a total of 640 readout channels, which were synchronously  
 97 acquired by means of two PETSys Front-End Board D version 2 (FEB/D-1024) modules, synchronized by means of a  
 98 Clock&trigger module that used LVDS signals at 400 Mbit/s<sup>25</sup>. The data-stream was read via SFP-connection to the PCI-  
 99 express acquisition board in the acquisition computer for its posterior analysis by dedicated reconstruction software. The  
 100 performance of the i-TED detectors for both Compton and PET imaging is described below in Methods within the section of  
 101 laboratory characterization of the i-TED based imaging system.

102 The proof-of-concept experiment was performed in cycles separated in well defined beam-on and beam-off periods. During  
 103 beam-on the  $\beta^+$  converter matrix was placed off-beam, as schematically shown in panel (a) of Fig. 2, thereby avoiding any  
 104 interfere of the matrix with the incoming proton beam. At this stage all samples under study were irradiated by the proton  
 105 particles at the same time and in similar amounts. Because of the proton-beam energy loss at each sample, different proton  
 106 energy ranges were covered at each slot position on the samples holder. The beam was fully stopped in the 2 mm thick graphite  
 107 layer, as schematically shown in both panels of Fig. 2. In the beam-on intervals PG Compton imaging is exploited by means  
 108 both i-TED modules, which could provide independent spatial information from the high-energy prompt gamma-rays emitted  
 109 from the different layers.

110 In the beam-off periods the cyclotron did not deliver any proton beam to the experimental room. At this point, the PLA  
 111 matrix was inserted using a remote mechanical actuator, as it is schematically shown in panel (b) of Fig. 2. In air, the mean free  
 112 path of  $\beta^+$  particles coming out from the unstable produced nuclei ranges up to a few cm due to the large Q-value of the decays  
 113 involved (mainly <sup>15</sup>O and <sup>11</sup>C)<sup>8-10</sup>. On the other hand, with the  $\beta^+$  converter matrix the mean free-path is significantly reduced  
 114 and most  $\beta^+$  particles annihilate in the vicinity of the unstable isotope, thus enabling also a precise PET imaging.

115 During the beam-off periods, in-beam PET is achieved by means of time-coincidences between the detectors of different  
 116 i-TED modules, whose field of view covers completely the volume of all the irradiated samples.

117 In the course of the proof-of-concept experiment, three different sample configurations and duty cycles were used. For sake

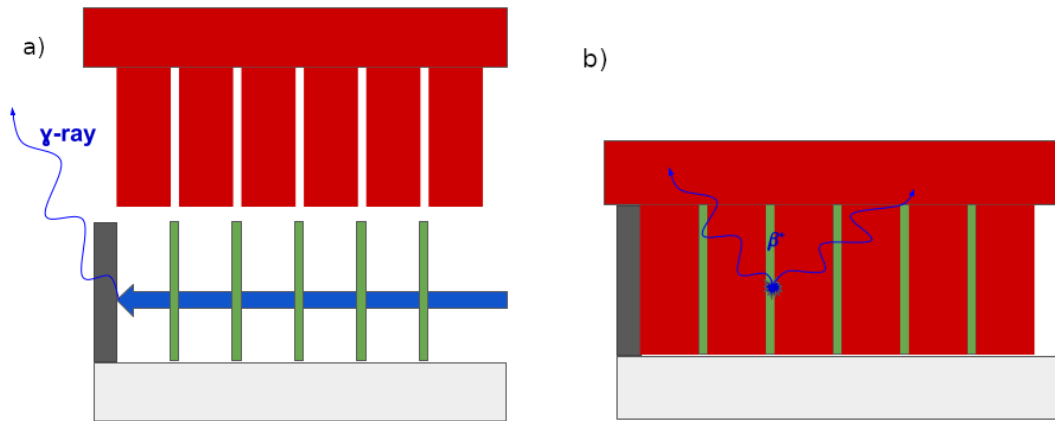


**Figure 2.** Schematic drawing of the experimental setup during the different part of the duty cycles. The thin layers under study are represented by green color, the thick graphite layer by gray and the PLA matrix by piece. Panel (a) shows the experimental setup during the beam-on period. In panel (b) is displayed the experimental setup during the beam-off period.

118 of clarity, in the following sections we refer to those configurations as the following:

- 119 • Configuration (I): Five Nylon layers and one thick graphite beam stopper.
- 120 • Configuration (II) Five Nylon layers and a graphite proton-beam energy degrader just before the Nylon samples.
- 121 • Configuration (III) Five PMMA layers and one thick graphite beam stopper.

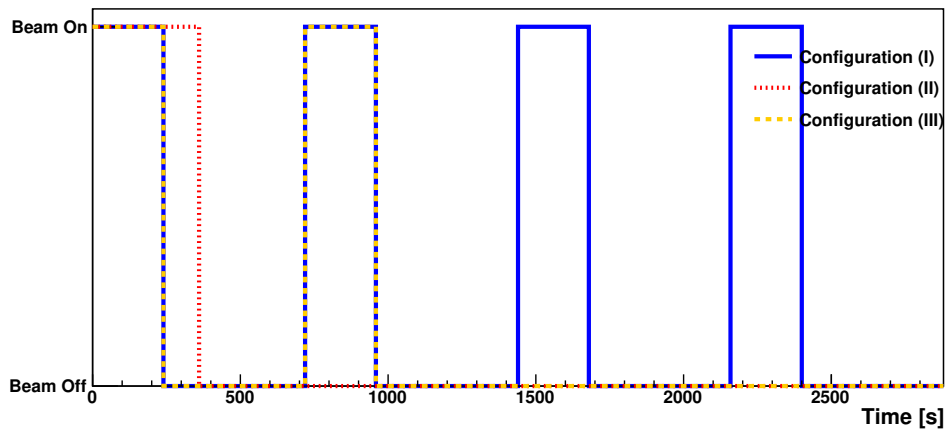


**Figure 3.** Schematic drawing of the experiment time structure used for the individual configurations used during the experiment. See text for details.

122 The time structure of beam-on and beam-off periods for each individual configuration are presented schematically by  
 123 different colors in Fig. 3. In the case of configuration (I), there was four duty cycles of 240 s beam-on followed by 480 s of  
 124 beam-off as displayed by blue-solid line. Configuration (II) consisted in one long irradiation of 360 s followed by a long time  
 125 period of beam-off as the red-dashed line shown. At last, for configuration (III), it was made of 2 beam-on periods of 240 s  
 126 time-spaced by 480 s followed by a long period of beam-off as the dashed-orange line represents.

127 The data reduction applied to the experimental data for the analysis of all the configurations is described below in the Data  
 128 reduction section in Methods.

## Results

In the following sections we show the results obtained for each one of the configurations listed above.

### Results for Configuration (I)

The configuration (I) consisted of five Nylon layers and a thick graphite layer at the end of the stack of samples. This section presents the results obtained for Compton- and PET-imaging in the beam-on and beam-off modes, respectively.

#### Compton imaging in the beam-on lapses

The Compton images reconstructed from the experimental data acquired with i-TED-A and i-TED-B during the beam-on lapses of configuration (I) are displayed in panels (a) and (b) of Fig 4. Panels (c) and (d) show the reconstructed MC images for i-TED-A and i-TED-B, respectively.

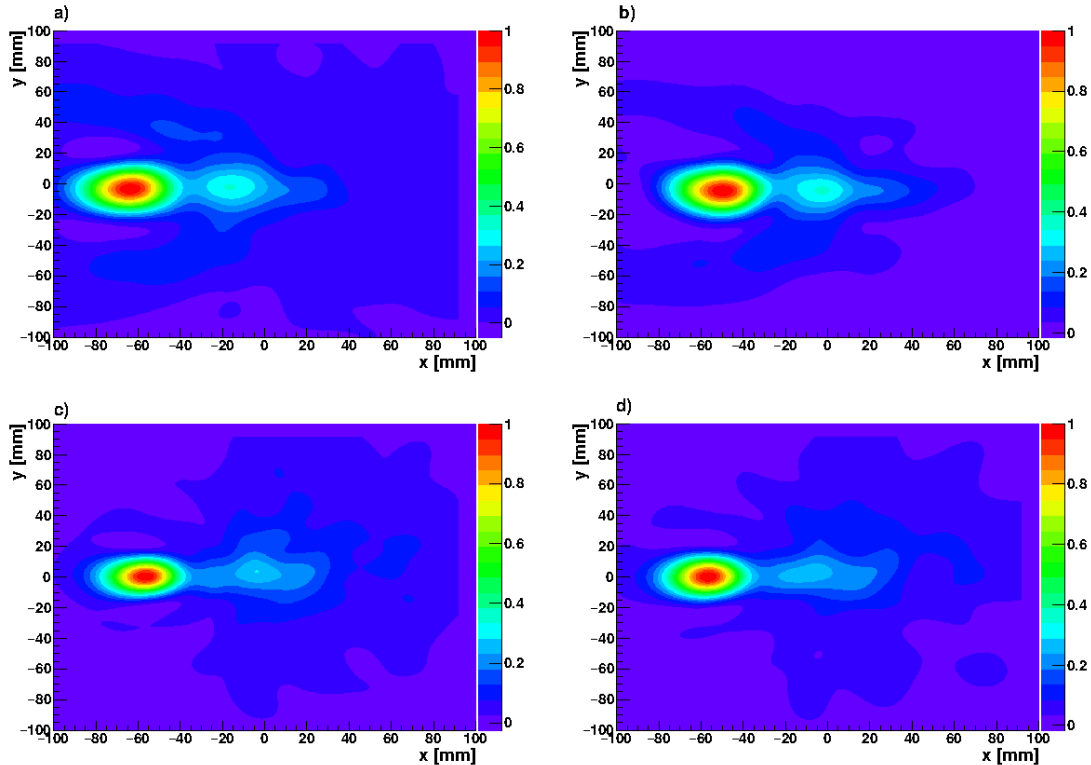


**Figure 4.** Reconstructed experimental and MC Compton images from PG  $\gamma$ -rays in configuration (I). See text for details.

The imaging reconstruction methodology is described below in the Methods section. As it can be observed in panels (a) and (b) of Fig. 4 the reconstructed experimental images for this configuration show a prominent maximum, which can be ascribed to prompt gamma-rays emitted from the thick graphite layer at the Bragg peak. A secondary maximum can be appreciated at the center of the image, corresponding to the geometrical center of the setup where detection efficiency is largest. The strength of these maxima depends on the different amount of material in each layer and the inelastic proton cross-section as a function of the proton energy. The fact that only the signature of the central Nylon layer can be observed indicates that detection efficiency and sensitivity are not enough to visualize the other four thin Nylon layers, as was to expect from the reduced thickness ( $800\mu\text{m}$ ). This statement is confirmed with the MC simulations. The MC images were reconstructed as the weighted superposition of the reconstructed MC images from the individual layers. The weighting values for each layer were calculated according to the amount of inelastic reactions with  $\gamma$ -rays spanning from 4 to 5 MeV registered at the individual layer in the dedicated proton MC simulation of this configuration.

The MC reconstructed images have a similar structure as the experimental ones, with a strong maximum at the graphite thick layer position and a second maximum in the central region of the image. If one compares the ratio between maxima in the experimental and MC images, the ratio changes from  $\sim 0.45$  down to  $\sim 0.35$ , respectively. This difference could be due to discrepancies between the evaluated cross-sections and/or stopping power present in the libraries (and hence on the MC results) and the actual real cross-section values.

154 **PET imaging in the beam-off lapses**

155 The 2D PET image reconstructed from the experimental data of i-TED-A and i-TED-B during the beam-off intervals for  
 156 configuration (I) is displayed in panel (a) of Fig. 5. The five irradiated layers can be clearly observed, well resolved from each  
 157 other. The maxima are well correlate with the position of the irradiated layers, as it is discussed below.

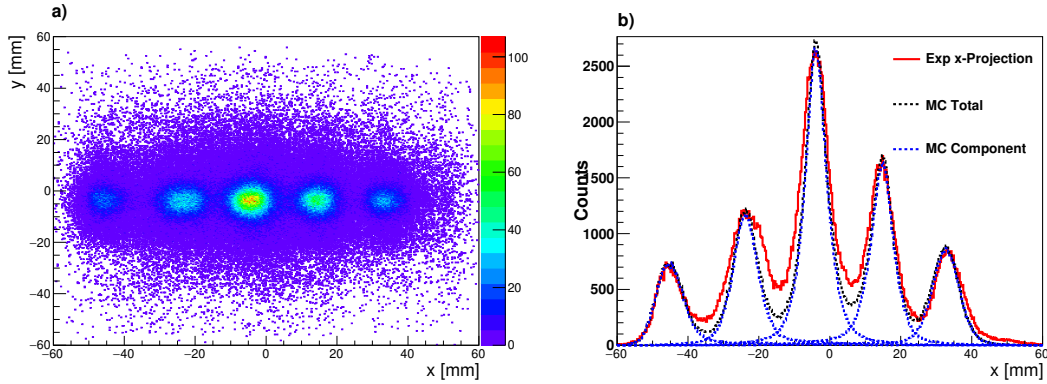


**Figure 5.** In panel (a), experimental 2D PET image for Configuration (I). Panel (b) 1D PET image x-projection (red) together with the Monte Carlo simulations of the individual contributions (blue) and total (black).

158 Panel (b) of Fig. 5 shows the x-axis projection of the experimental image (red) together with a MC simulation of the  $\beta^+$   
 159 emission of the activated layers (black). The MC image was reconstructed by weighting the PET images obtained from the  
 160 simulation of the individual layers. The contribution of each layer is represented in Fig. 5 by a dashed-blue line. The spatial  
 161 distribution used for the MC calculation is described in the Methods section below. The weight of each individual contribution  
 162 was chosen to match the height of the reconstructed experimental distribution.

163 While the experimental distributions for the first, second and last sample slots are relatively well reproduced by the MC  
 164 simulations, the third and fourth distribution positions are slightly broader than those reconstructed from the MC calculations.  
 165 A plausible explanation for this effect might be that the PLA matrix did not fit these two layers perfectly, and thus the mean free  
 166 path of the  $\beta^+$  particles coming out from those irradiated layers was larger, thus leading to an additional broadening of the  
 167 measured distributions at those locations.

168 Tab. 1 shows the results obtained from a Gaussian fit of the experimental x-axis distribution of this configuration. The first  
 169 column indicates the Nylon sample position. The second and third columns show the peak positions and widths ( $\sigma$ ). The last  
 column contains the widths ( $\sigma$ ) from a Gaussian fit of the MC distribution at the corresponding positions.

Nylon sample	x [mm]	$\Delta x$ [mm]	$\sigma_{Exp}$ [mm]	$\sigma_{MC}$ [mm]
1	33.46(4)	-0.46(4)	4.16(4)	4.22
2	14.33(3)	0.67(3)	4.41(3)	4.03
3	-4.06(2)	-0.06(2)	4.22(2)	3.94
4	-23.11(3)	-0.89(3)	5.53(4)	4.17
5	-45.29(6)	-0.71(6)	4.07(7)	3.99

**Table 1.** Experimental Gaussian fit of the PET x-projection for configuration (I). The last column shows the widths obtained from the MC distributions.

170 These results thus confirm an overall fair agreement between simulation and experiment. It is worth to highlight the  
 171 complementary performance of Compton and PET imaging in terms of detection sensitivity and spatial resolution, which  
 172 indicates that a smart combination of both approaches in a convenient beam-time structure can result in an overall improvement  
 173 of the ion-range assessment.  
 174

175 **Results for Configuration (II)**

176 In this section we describe the results for the configuration (II), corresponding to five Nylon layers and a proton-beam energy  
 177 degrader placed just before the samples holder. This is an interesting configuration because of the low beam energy (17 MeV at  
 178 the first Nylon layer).

179 **Compton imaging in the beam-on lapses**

180 The experimental reconstructed Compton images for i-TED-A and i-TED-B modules obtained for the configuration (II) are  
181 displayed in panels (a) and (b) of Fig 6. In the same figure, panels (c) and (d) shown the reconstructed MC images for i-TED-A  
182 and i-TED-B, respectively. Both, experimental and MC images were reconstructed following the same procedure described in  
183 the previous section.

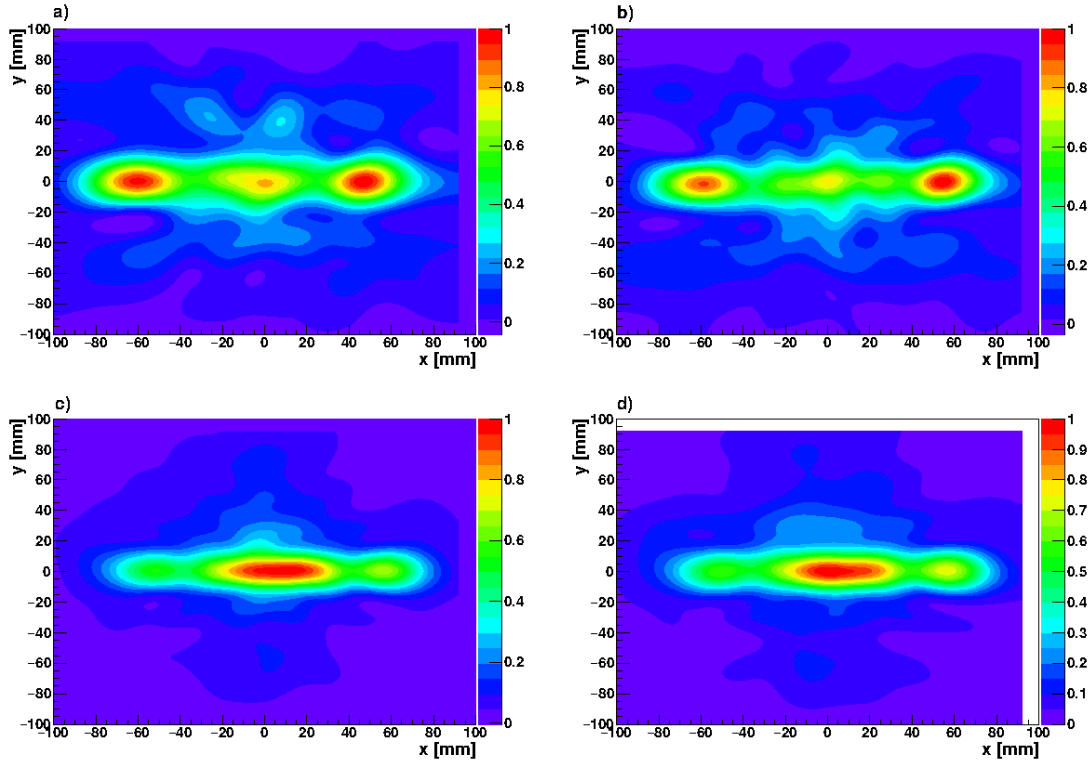


**Figure 6.** Compton images from PG  $\gamma$ -rays in configuration (II). See text for details.

184 For this specific configuration the experimental images of both i-TED modules show two intense emission maxima, with  
185 comparable strengths, at both extreme x-positions of the field of view. The first maximum on positive x-values agrees well with  
186 the location of the graphite degrader. The second maximum on the left-hand side (negative x-values), is situated at the same  
187 position of configuration (I), which is therefore consistent with the position of the thick graphite layer or beam stopper. In  
188 addition, in the center of the image one can appreciate another maximum, with an strength that is  $\sim 20\%$  lower than the two  
189 main lateral peaks.

190 Interestingly, in this configuration the reconstructed MC images do not reflect what is observed experimentally. The images,  
191 for both i-TED modules show a maximum in the central part of the image, where the Compton detection efficiency is maximum.  
192 It is worth to mention that between the central part and the positions where the thick graphite stopper and degrader are placed  
193 there is a difference of about  $\sim 30\%$ . Almost the same value but in the opposite direction compared to the experimental images.  
194 At this moment we can only ascribe this notable discrepancy to possible deficiencies in the cross-sections present in the  
195 evaluated libraries, especially at low proton energies.

196 **PET imaging in the beam-off lapses**

197 The reconstructed experimental 2D PET image from the beam-off intervals of configuration (II) is displayed in panel (a) of  
198 Fig. 7. As for the case of the beam-on results, the obtained images are really interesting; In addition to the five Nylon layers,  
199 the  $\beta^+$  annihilation events at the entrance energy degrader is well observed at the right-hand side of the image ( $x=58$  mm), a  
200 position which is close to the edge of the PET field of view between both i-TED modules.

201 Panel (b) of Fig. 6 shows the x-axis projection of the experimental 2D PET image (red) and the MC simulation of the  
202 irradiated layers (black), in a similar fashion as it was made for configuration (I). The contribution of the individual layers is  
203 displayed in the same figure by a dashed-blue line. The MC distribution was also scaled to match the experimental distribution.  
204 The position of the layers in the geometry of the MC simulations was set to the same position of configuration (I). Actually,  
205 the the first and the last layer positions are reconstructed in the same position as configuration (I), a situation which does not

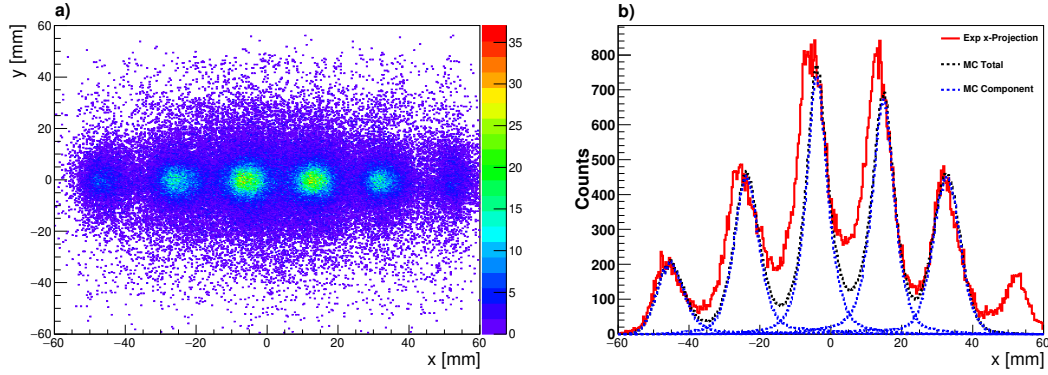


**Figure 7.** Experimental 2D PET image for Configuration II (a). PET image x-projection (red) together with the MC simulations of the individual images (blue) and the total MC distribution (black) are shown in panel (b).

occur for the second, third and fourth layers. This change may indicate a small displacement in experimental setup during the exchange of the irradiated layers. Also a small change in the direction of the proton beam after restarting the cyclotron irradiation should not be rejected.

As it was found for configuration (I), the obtained experimental width of the individual layers compared to the MC distributions seems to be larger (in average by 15%) for layer positions two, three and four.

The experimental distributions were fitted to Gaussian functions. The reconstructed position and widths ( $\sigma$ ), together with the MC widths are presented in Tab. 2.

Nylon sample	x [mm]	$\Delta x$ [mm]	$\sigma_{Exp}$ [mm]	$\sigma_{MC}$ [mm]
1	32.28(5)	0.72(5)	4.19(5)	4.23
2	13.15(4)	1.85(4)	4.4(4)	4.040
3	-5.35(4)	1.35(4)	4.57(5)	3.95
4	-24.71(5)	0.71(5)	5.02(6)	4.17
5	-46.5(2)	0.5(2)	4.1(2)	4.0

**Table 2.** Position and widths obtained by fitting a Gaussian function to the PET x-projections in configuration (II). The last column shows the width values obtained for the MC simulations.

Comparing the results of Tab. 2 with those obtained for configuration (I) in Tab. 1, the position of the second, third and fourth layers show a change of  $\sim 1$ mm, thus reflecting the good sensitivity of the PET imaging to the details of the experimental setup. As expected from the panel (b) of Fig. 7, the experimental and MC widths for the first and last layer are in good agreement, while for the second, third and fourth layer the experimental values are larger by 15%.

### Results for Configuration (III)

This section presents the results for the last set-up, configuration (III), corresponding with the irradiation of five PMMA layers. In this case no beam energy degrader was placed between the entrance window of the cyclotron and the samples holder.

#### Compton imaging in the beam-on lapses

The reconstructed experimental Compton images from prompt  $\gamma$ -rays for i-TED-A and i-TED-B during the beam-on intervals of configuration (III) are displayed in panels (a) and (b) of Fig 8. Panels (c) and (d) show the reconstructed MC images for the same modules.

As for configuration (I), the experimental Compton images reconstructed for both i-TED modules exhibit a main peak located at the position of the thick graphite layer and a second (smaller) maximum close the geometrical center of the experimental setup, in agreement with the location of the maximum Compton detection efficiency.

The reconstructed MC images, calculated in the same way as for previous configurations (I) and (II), show the strong emission peak at the thick graphite beam stopper. The secondary peak shows a double-peak structure that the experimental image does not have. In terms of relative intensities of the main and secondary peaks, the agreement between experiment and simulation is satisfactory. The ratio of intensities ranges from  $\sim 0.3$  for the experimental image to  $\sim 0.25$  for the MC.

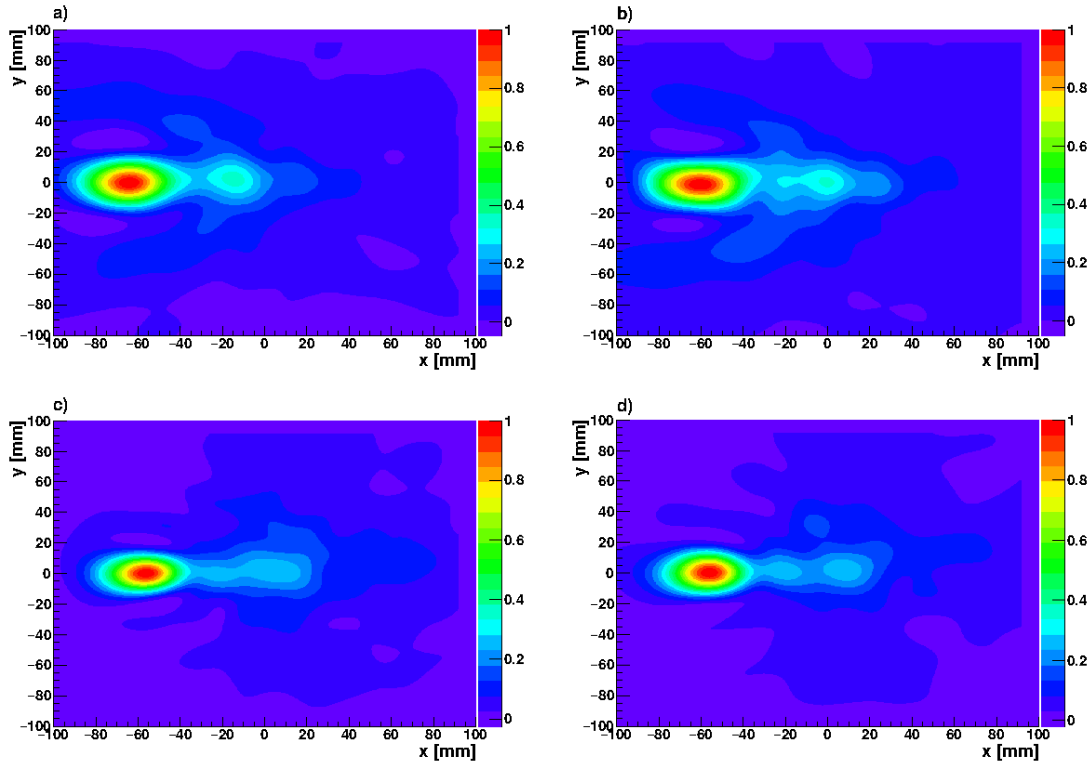


**Figure 8.** Compton images in configuration (III). See text for details.

231 **PET imaging in the beam-off lapses**

232 The reconstructed experimental 2D PET image for this configuration during the beam-off period is displayed in panel (a)  
 233 of Fig. 9. As for the previous configurations, the five layers can be clearly resolved and located at the true positions, thus  
 234 demonstrating the fidelity of the PET imaging of the experimental setup for this type of measurements.

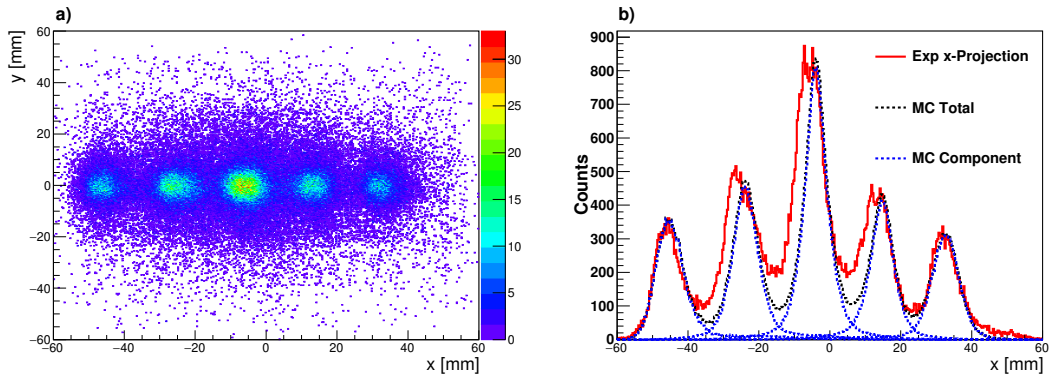


**Figure 9.** Experimental 2D PET image for Configuration (III) is shown in panel a). Panel b) shows the 1D PET image x-projection (red) together with the Monte Carlo simulations of the individual images (blue) and the total (black).

235 Panel (b) of the same figure shows the experimental PET x-axis projection (red) together with a MC simulation of the of the  
 236 activated layers (black), in a similar way as it was calculated for the rest of configurations. The MC distributions, as in the  
 237 previous sections, were also scaled to match with the height the experimental data, keeping the same positions as configuration  
 238 (I).

239 The x-axis projections show that the results for this configuration have the same pattern than configurations (I) and (II).  
 240 The MC distribution matches very well the first and the last irradiated layers, while the experimental data of the central layers

241 are broader and moved from what is expected from the MC simulations. The apparent position of the layers has the same  
 242 displacement as in configuration (II) respect to (I), 1 mm. The fact that configuration (II) and (III) were performed one after the  
 243 other in the second day of the experimental campaign could support the possibility that the proton beam was not impinging in  
 244 the same exact position as for configuration (I).

245 Gaussian fits were performed for the x-axis distribution and the results are presented in Tab. 3

PMMA sample	x [mm]	$\Delta x$ [mm]	$\sigma_{Exp}$ [mm]	$\sigma_{MC}$ [mm]
1	32.34(5)	0.66(5)	4.09(6)	4.22
2	12.82(5)	2.18(5)	4.76(6)	4.03
3	-5.67(3)	1.67(5)	4.39(4)	3.91
4	-24.93(5)	0.94(5)	5.20(6)	4.15
5	-46.1(1)	0.1(1)	4.0(1)	4.0

**Table 3.** Positions and widths ( $\sigma$ ) obtained for the experimental PET x-projection for configuration (III). The last column shows the values obtained for the MC simulations.

246 The same pattern is observed for this configuration regarding the width of the distributions. The first and the last irradiated  
 247 layers agree very well with each other. For the rest of layers the experimental width is slightly broader. This fact may again  
 248 support the hypothesis that the PLA matrix did not fill completely the gaps of the central layers in the sample holder.

## 249 Discussion and Conclusion

250 In this work we have demonstrated the possibility to use modular Compton cameras in a front-to-front and synchronous  
 251 configuration in conjunction with a pulsed proton beam to perform quasi-simultaneous in-beam PET and prompt gamma-ray  
 252 Compton imaging. This pilot experiment comprised a variety of materials and configurations, thereby aiming at addressing the  
 253 systematic spatial uncertainties related to each one of the imaging techniques.

254 The PET spatial resolution obtained in this study is reported in Tab. 6 of the Methods section. The resolution is in agreement  
 255 with the one calculated by means of MC simulations using individual crystal position reconstructions reported in a previous  
 256 work<sup>19</sup>, and in line with similar pre-clinical PET-imaging prototypes (5-6 mm) reported in<sup>7</sup> and references therein. The  
 257 repeatability performance of our PET system is given by the  $\Delta x$  differences between measured maxima and reference MC  
 258 values for the target layers, as reported in tables 1, 2 and 3. Maximum deviations of about 2 mm were found, with average  
 259 deviations typically within  $\sim 1$  mm or less. It is worth to mention that, at variance with our detection set-up, other PET works  
 260 use smaller and thinner scintillation crystals, where pin-cushion and non-linearity effects are less severe<sup>19</sup>. However, a high  
 261 efficiency is required when aiming at online monitoring, and also thick scintillation crystals are required to image high-energy  
 262 prompt gamma-rays. The virtue of PET for ion-range monitoring is the attainable spatial sensitivity, resolution and repeatability.  
 263 However, these advantages are shadowed by the fact that it can be hardly accomplished during beam irradiation and it requires  
 264 also of a certain beam-off time-lapse for the  $\beta^+$  emitters to decay and acquire sufficient counting statistics. The latter drawbacks  
 265 directly affect the total treatment time and increase the blurring due to wash-out effects.

266 The experimental PG Compton images were compared with the MC simulations of the different configurations and the single  
 267 graphite layer in Fig. 4, 6, 8 and later in Fig. 17 of the Methods section. The image resolutions between both experimental and  
 268 MC results are comparable, thus yielding an average spatial resolution of about 24 mm for both imagers. Small discrepancies  
 269 observed during the irradiations between main and secondary peaks may point to deficiencies in nuclear cross-section data  
 270 included in the evaluated libraries commonly used for MC simulations. This result for the spatial resolution cannot be directly  
 271 compared with other works, as it strongly depends on the geometry of the set-up and the distance to the object under study.  
 272 The repeatability of the reconstructed Compton images can be estimated from the position of the maximum for each imager  
 273 and configuration (table 4). Deviations of 2 mm were found, with an average value of about 1 mm, which is slightly worse  
 274 than that obtained with PET. However, deviations of almost 8 mm are found for the Compton reconstructed positions of the  
 275 configuration II, when compared to the other two configurations. This effect is not fully understood yet, but it may indicate that  
 276 the repeatability of the Compton reconstruction is more sensitive than PET to variations in beam energy or other experimental  
 277 effects. On average, both resolution and repeatability are better in PET than in Compton imaging. Rather than the angular or  
 278 spatial resolution itself, it is the sensitivity of the imaging apparatus to range shifts or variations what matters when it comes to  
 279 addressing range verification<sup>18</sup>. The latter is more related to repeatability than resolution, although a higher image resolution  
 280 is expected to deliver also a more reliable range monitoring. Still, one of the main advantages of Compton imaging is its  
 281 suitability to carry out range verification in-situ and in real-time. From our pilot experiment the real-time capability of each  
 282 imaging approach can be inferred from the average count rates in- and off-spill for each sub-system. These values are reported  
 283 below in table 5. On average, a factor 300 higher counting rate is registered in-spill for Compton imaging, when compared to

i-TED	Configuration Max. Position in Compton (mm)		
	(I)	(II)	(III)
A	-71.17	-63.50	-70.50
B	-68.8	-64.16	-71.16
$\Delta x$	2.3	0.66	0.66

**Table 4.** Maximum emission position for Compton imaging (in mm) in the three configurations and both i-TED modules. The bottom line shows the differences between maxima, which reflect the repeatability of the measurement.

	Configuration Avg. Count Rate (Counts/s)		
	(I)	(II)	(III)
Compton in-spill	13324	6642	14975
PET off-spill	61	29	20

**Table 5.** Average count rates for Compton imaging in-spill and for PET imaging off-spill.

284 off-spill with the PET technique. Therefore, to achieve a similar statistical accuracy with both imaging methods, a pulsed beam  
 285 with a duty-cycle of 0.01, or smaller, becomes convenient.

286 In summary, to a large extent both PET and PG Compton are rather complementary approaches and may be used in a  
 287 synergic fashion. Therefore, the possibility to combine them in a single and dedicated system, similar to the one reported here,  
 288 seems a reasonable step forward towards attaining high accuracy range verification (PET) in real-time (Compton). In this  
 289 respect, one of the main limitations of the present work was the low beam energy (18 MeV), when compared to clinical values  
 290 (100-200 MeV). For this reason the beam on/off lapses used in this work had to be significantly large, of several 100 s and a  
 291 special target or phantom had to be employed. Next steps to develop further the approach proposed here comprise the realization  
 292 of measurements using average clinical beam conditions and conventional water or PMMA phantoms. Using a pulsed beam of  
 293 a high energy with a large phantom and a suitable duty cycle, it may become possible to correlate sequential PG-Compton  
 294 and PET-images in- and off-spill, respectively. There are two main aspects to research in the future experiment. First, the  
 295 performance of the detection system at the high counting rate conditions of the high-energy and high-intensity clinical beams  
 296 needs to be validated. Second, one has to determine which is the optimal duty-cycle for the proton beam to accomplish both  
 297 PG Compton and PET imaging for a proper trade-off of statistical and systematic accuracy. The aforesaid pulsed-beam  
 298 duty-cycle requirement of less than 0.01 aligns very well with the application of this new methodology in treatments with  
 299 superconducting synchrocyclotrons, which produce a pulsed beam (few  $\mu$ s, every 1–2 ms)<sup>26</sup>, and also with recent developments  
 300 related to hybrid delivery approaches in flash therapy<sup>27</sup>.

## 301 Methods

### 302 Data reduction

303 The individual detectors of each i-TED module were calibrated in energy using a point-like <sup>152</sup>Eu  $\gamma$ -ray source. In addition to  
 304 the  $\gamma$ -ray lines corresponding to the strongest nuclear reactions identified during the proton irradiations at CNA were included  
 305 in the energy calibration. The latter correspond to the <sup>12</sup>C(*p,p'*) $\gamma$ <sup>12</sup>C and <sup>16</sup>O(*p,x*) $\gamma$ <sup>12</sup>C nuclear reactions, both emitting 4.4  
 306 MeV  $\gamma$ -quanta<sup>6</sup>. The corresponding first and second escape peaks were also clearly visible and included in the calibration, as  
 307 well as the 511 keV  $\gamma$ -ray from the detection of  $\beta^+$  annihilation events during the beam-on periods. A third polynomial degree  
 308 was used to model the energy-ADC relation over this large energy range. An example of the individual energy calibration is  
 309 displayed in Fig. 10. The experimental ADC values for the different  $\gamma$ -ray transitions are represented by red markers, while the  
 310 fitted polynomial is displayed by the dashed-blue line.

311 The energy detection thresholds obtained for i-TED-A and i-TED-B were of 100 keV to 250 keV, respectively. The  $\gamma$ -ray  
 312 interaction positions in the individual PSDs were reconstructed following the procedure described in<sup>19</sup>. The absolute  $\gamma$ -ray  
 313 position interaction was obtained from the reconstructed intrinsic 3D position coordinates and the location of each PSD, which  
 314 was well known by set-up construction.

315 The i-TED energy-calibrated add-back time-coincidence spectra between detection planes registered during the beam-on  
 316 period of configuration (I) is displayed in Fig. 11. The spectra of i-TED-A and i-TED-B are represented by the blue and red  
 317 lines, respectively. The time-coincidence window between different detection planes is 10 ns, which allowed to reduce random  
 318 coincidences with other background sources. The deposited energy spectra registered during the three different configurations  
 319 were similar in size and shape. This result might indicate the registered spectra are dominated by the inelastic reactions in  
 320 Carbon isotopes at the thick graphite layer, an effect which is expected from the Bragg curve<sup>2,5</sup> and the large amount of material

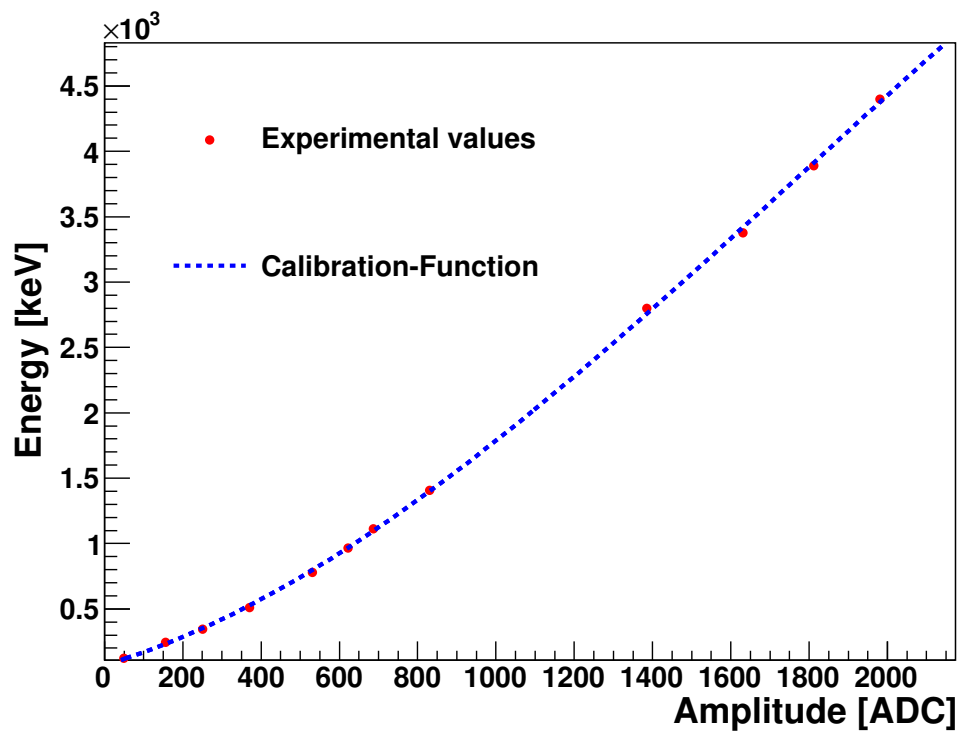


**Figure 10.** Energy calibration for an individual detector of i-TED-A. The experimental data from the  $^{152}\text{Eu}$  calibration source and  $\gamma$ -ray lines PG identified during beam-on periods are represented by the red dot points. The fitted third degree polynomial is plotted by the dashed blue line.

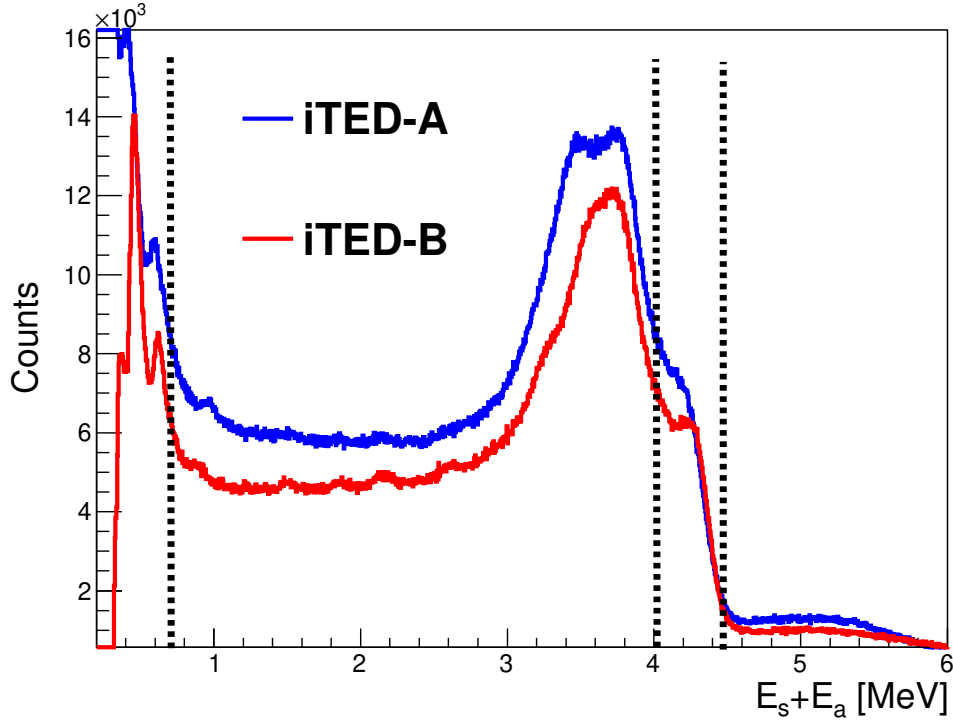


**Figure 11.** Add-back deposited energy detected by i-TED-A (blue) and i-TED-B (red) during the beam-on period. The dashed lines correspond to the energy threshold for imaging and the 4.4 MeV  $\gamma$ -ray line used for Compton imaging.

321 of the thick graphite target when compared to the thin samples of Nylon and PMMA.

322 The energy window of 4.0-to-4.6 MeV chosen for the beam-on periods to perform Compton imaging is displayed by dashed  
 323 lines in Fig. 11. A high energy threshold for the individual absorber PSD detectors, 700 keV, was used for the Compton imaging  
 324 reconstruction aiming at reducing artifacts in the images due to time-correlated pair production events and random coincidences  
 325 with 511 keV. The image plane chosen for the Compton reconstruction corresponds to the axial direction of the samples  
 326 holder, i. e. 8.5 cm from the frontal face of the i-TED-A module. Finally, the Compton images in this work were obtained by  
 327 implementing the analytical inversion algorithm based on spherical harmonics developed by Tomotani and Hisarawa in 2002<sup>28</sup>.  
 328 This inversion formula, which is based on an infinite Legendre polynomial expansion, leads to an approximate solution given  
 329 by a unit vector in the image space,  $\vec{s}$ . The image at that vector position is described by

$$f(\vec{s}) \approx \int_{\cos\omega_{min}}^{\cos\omega_{max}} d\cos\omega \int_S d\vec{t} k^{-1}(\vec{t}, \vec{p}; \cos\omega) g(\vec{t}; \cos\omega), \quad (1)$$

where  $\vec{t}$  is a unit vector into the projection space,  $\omega_{min}$  and  $\omega_{max}$  are the minimum and maximum Compton scattering angles that can be measured with the i-TED modules configuration,  $g(\vec{t}; \cos\omega)$  is the projection data in the image space and  $k^{-1}(\vec{t}, \vec{p}; \cos(\omega))$  is the inversion kernel. This kernel is defined as

$$k^{-1}(\vec{t}, \vec{p}; \omega) = \sum_{n=0}^{N_{max}} \frac{2n+1}{4\pi H_n} P_n(\cos\omega) P_n(\vec{s} \cdot \vec{t}) \quad (2)$$

330 with  $H_n$  given by the formula

$$H_n = \int_{\cos\omega_{min}}^{\cos\omega_{max}} \sigma(\cos\omega) P_n^2(\cos\omega) d\cos\omega. \quad (3)$$

331 In the latter expression  $P_n$  is the Legendre polynomial of order  $n$  and  $\sigma(\cos\omega)$  is the Klein-Nishina Compton differential  
 332 cross-section<sup>29</sup>.  $N_{max}$  is the maximum number of terms involved in the polynomial expansion and it must be chosen according

333 to the angular resolution of the experimental apparatus, i.e., the experimental angular resolution of the i-TED modules that  
 334 depends on the selected deposited energy window and the distance between detection planes.

335 The complexity of this algorithm leads to a large computational cost in order to reconstruct a Compton image with sufficient  
 336 accuracy. For this reason, the algorithm was implemented in this work for GPU devices using the CUDA toolkit<sup>30</sup>. This  
 337 methodology allows for a speed-up factor of about  $\sim 121$ , when compared to the single-threaded CPU version. Additionally,  
 338 and aiming at quasi-real time image reconstruction in clinical studies,  $H_n$  was pre-computed for a wide range of  $\gamma$ -ray energies  
 339 and Compton scattering angles corresponding to the range of  $\omega_{min}$  and  $\omega_{max}$  detectable by the i-TED modules. Thus, the  $H_n$   
 340 values were saved in a table format for its posterior use, enhancing further the speed of the image reconstruction. More details  
 341 can be found in Ref.<sup>18</sup>.

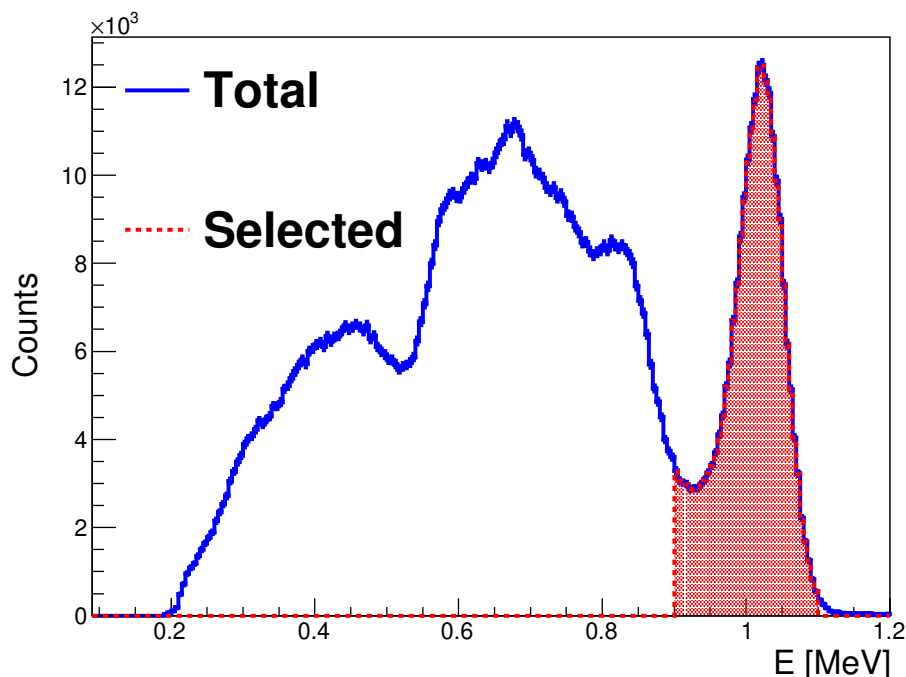


**Figure 12.** Add-back deposited time-coincidence energy spectrum of the i-TED modules during the beam-off period. The selected deposited energy window for PET imaging is displayed by the shadowed red region.

342 The add-back energy-calibrated energy spectrum between detectors of the different i-TED modules during the beam-off  
 343 period is displayed in Fig. 12. The total add-back spectrum is displayed in blue, while the selected window for the  $\beta^+$   
 344 full-energy coincidence peak used for PET imaging is shown by the shadowed red region. The spectra were obtained in  
 345 time-coincidence between the individual detectors of different i-TED modules using a coincidence time-window of 10 ns. This  
 346 time window, the same than the one used for the individual i-TED detection planes, was chosen owing to the fast time response  
 347 of the system and the distance between i-TED modules.

348 The PET images were reconstructed using a simple analytical algorithm, where straight lines of response (LOR) between  
 349 the  $\gamma$ -ray interaction positions at the different detectors of the i-TED modules were intersected with the central axial plane. The  
 350 latter PET imaging plane coincides with the one used for Compton imaging during in the beam-on periods, which was at 85 mm  
 351 from the front face of the i-TED-A module.

352 A detailed geometry of the experimental setup was implemented in a C++ Monte Carlo (MC) application based on the  
 353 GEANT4 toolkit, version 4.10.6<sup>31</sup>. In the MC simulation included the standard electromagnetic package option 3, the radioactive  
 354 decay, and the packages commonly used in hadron-therapy simulations<sup>32</sup>. These calculations were intended to interpret and  
 355 cross-check the experimental results obtained for the different configurations, as it is described below in sections , and . A  
 356 figure of the geometry implemented in the MC code is displayed in Fig. 13. For Compton imaging it includes the two i-TED  
 357 modules, the sample holder with the samples and the thick graphite layer. For PET imaging the geometry includes also the  
 358 PLA converter matrix, not shown in Fig. 13. In the simulations, the intrinsic PSD reconstruction resolutions for both position  
 359 and energy-response were included according to the laboratory characterization described in the references<sup>19,33</sup>. The energy  
 360 dependence of the energy resolution,  $R(E)$ , was determined from the energy calibration procedure using a functional of the

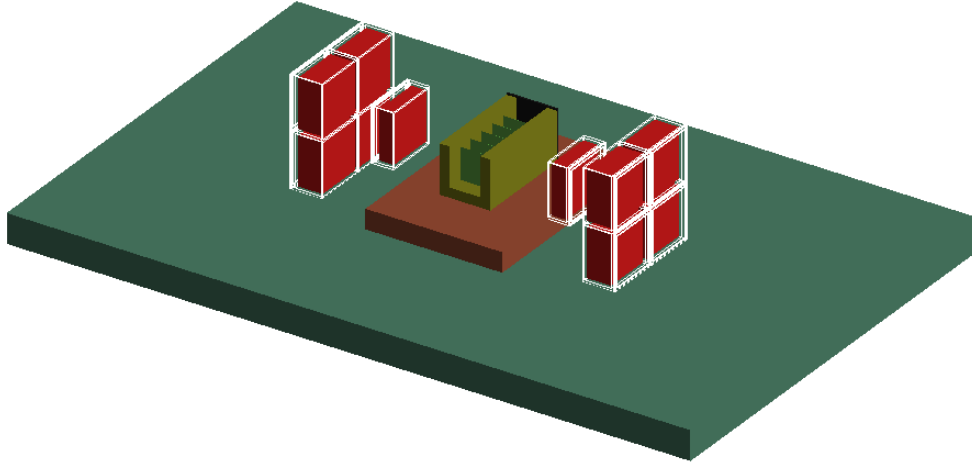


**Figure 13.** Geometry of the experimental setup as implemented in the MC simulation. See text for details.

361 form

$$R(E) = \sqrt{a + b/E}, \quad (4)$$

362 where  $a$  and  $b$  are parameters adjusted from the experimental energy calibrations. For the sake of a realistic comparison, the  
 363 MC-calculated Compton- and PET-images were reconstructed by implementing exactly the same algorithms and conditions  
 364 applied to the experimental data.

365 A further consideration is required regarding the effect of the proton-beam divergence. As protons interact with the sample  
 366 material along the beam path a spreading is introduced in the transversal spatial profile of the beam. Because the Compton- and  
 367 PET-imaging algorithms used in this work are based on a single 2D image plane for the reconstruction, the images obtained will  
 368 reflect also the spreading due to beam straggling effects. In order to account for this experimental effect a dedicated simulation  
 369 of the proton beam passing through the stack of samples was performed for the three different configurations. This calculation  
 370 included the different materials and positions in the experimental setup, as shown in Fig. 13. For each simulation study the 3D  
 371 vertex-positions of the inelastic proton scatterings at the different irradiated layers were registered. As an example, Fig. 14  
 372 shows the proton-beam profile calculated at the graphite layer in configuration (I). These distributions will be used afterwards  
 373 as initial emission-vertex distributions for the PG  $\gamma$ -rays and  $\beta^+$  particles in the beam-on and beam-off modes, respectively.  
 374 The full-width-at-half-maximum (FWHM) values of the proton beam distribution calculated for the different irradiated layers is  
 375 displayed in Fig. 15. Configurations (I) and (II) show similar beam spreads at each individual layer for both the Nylon and  
 376 PMMA material. This was expected because both materials have similar composition and densities. For the configuration (II)  
 377 the beam profile is much broader due to the effect of the graphite proton-beam degrader just before the sample holder, which  
 378 increases the width of the incoming proton beam reported in the subsequent sections.

379 Finally, for the sake of clarity it is worth to indicate that for both, PET and Compton imaging, the reconstruction is made  
 380 from the reference system or point-of-view of i-TED-B. Thus, the direction of the beam in the images is from the left- to the  
 381 right-hand side for all the images, being the left-hand side the position of the thick graphite layer and the right hand side the  
 382 entrance of the proton beam as it schematically shown in panel (a) of Fig. 2.

383 The above considerations are taken into account in the comparison between simulated and experimental data, which are  
 384 described for both PET and Compton images in the following sections.

### 385 **Laboratory characterization of the i-TED based imaging system**

386 In this section we report on the performance of the two i-TED system for Compton and PET imaging by comparing MC  
 387 simulations with experimental data for point-like radioactive sources. The goal of this work is to characterize the systematic  
 388 behaviour of our detection set-up, as a preceding step to the in-beam PET and Compton imaging application.

#### 389 **PET imaging**

390 The PET performance was experimentally characterized by using a standard point-like  $^{22}\text{Na}$  calibration source placed at the  
 391 sample-holder slot positions number two, three and four. These positions match with the central region of the imaging system

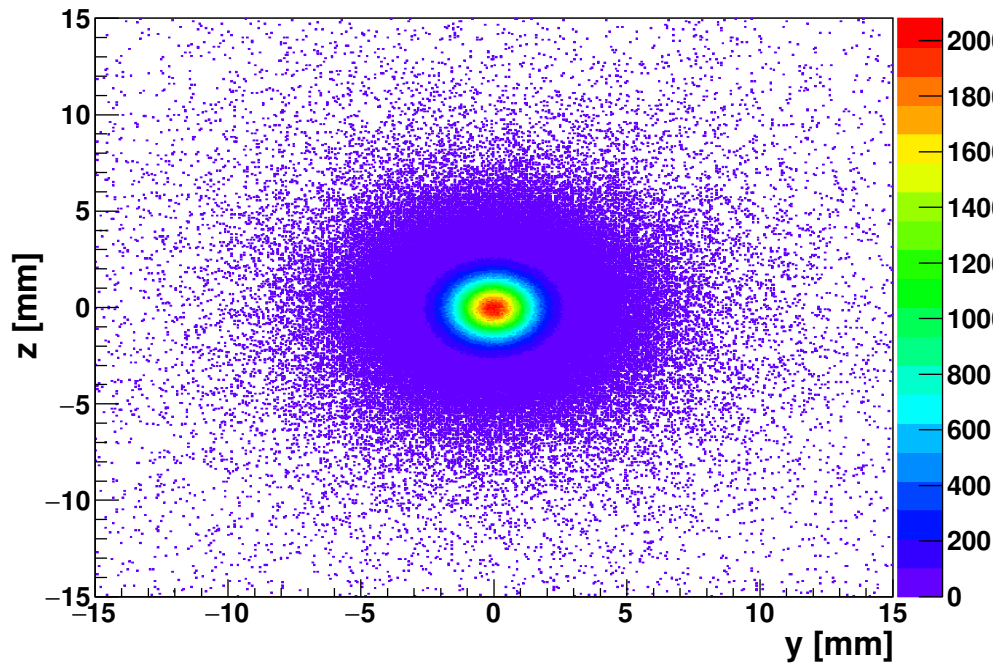


Figure 14. Example of MC proton spatial beam profile registered in the thick graphite layer for configuration (I).

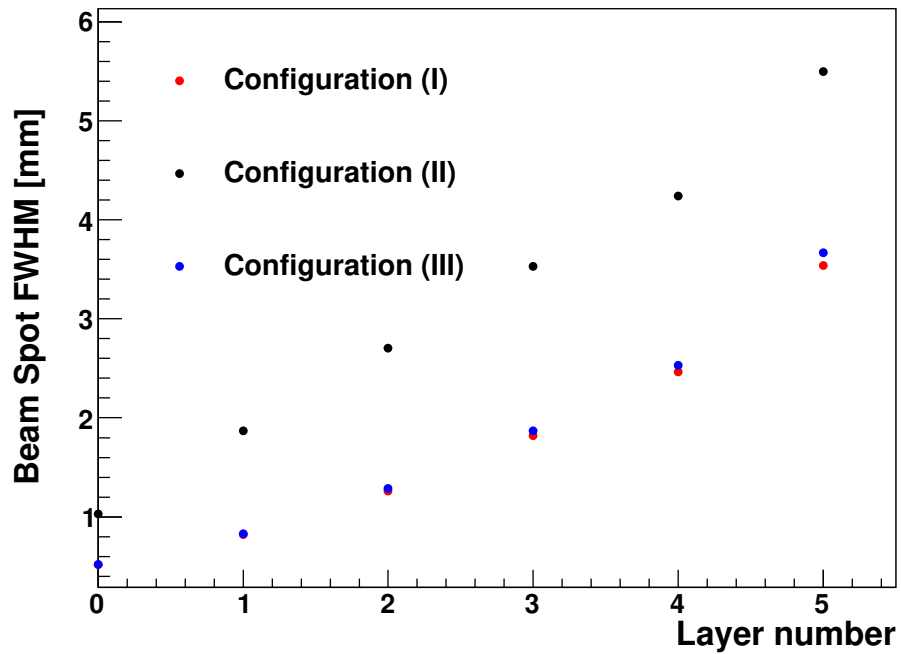
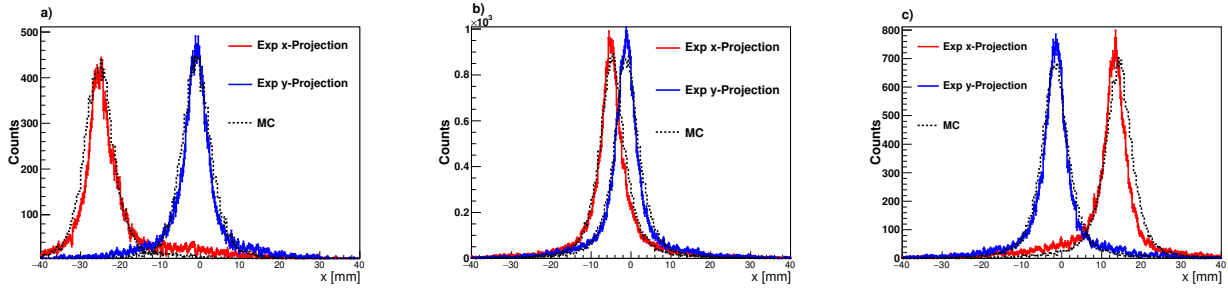


Figure 15. MC FWHM of the proton beam spatial distribution at the different layers for the different configurations.



**Figure 16.** x- (red) and y-axis (blue) projections of the PET images for the  $^{22}\text{Na}$  calibration source at different positions along the sample holder. The result of the MC simulation is shown by the dashed-black curve. Panels (a), (b) and (c) correspond to slots number four, three and two in the sample holder.

392 and cover the entire PET field of view between the scatter planes of both i-TED modules. The  $^{22}\text{Na}$  sample was placed at the  
 393 axial-beam distance, thereby matching well the Compton and PET reconstruction planes.

394 Projections of the obtained PET distributions along the x- and y-axis for the different slot positions are displayed in Fig. 16  
 395 by the red (x) and blue (y) lines, respectively. In the same figure, the black-dashed line shows the MC results from the simulation  
 396 of the point-like  $^{22}\text{Na}$  source.

397 A fair agreement is obtained between the experimental results and the MC simulations for all positions. The MC simulations  
 398 were scaled to match the height of the experimental distributions. In particular, the results for the slot number four are displayed  
 399 in panel (a) of Fig. 16. The x-coordinate of this position is found to be especially sensitive to pin-cushion effects, since this  
 400 position is close to the limit of the field-of-view between the scatter planes of both i-TED modules ( $50 \times 50 \text{ mm}^2$ ). The good  
 401 agreement found between simulation and experiment indicates that pin-cushion effects are properly treated in the reconstructed  
 402 positions by means of the SVM-method<sup>19</sup>. For the y-axis the agreement between the experimental and MC distributions is  
 403 also satisfactory. Panel (b) of the same figure shows the results obtained for the  $^{22}\text{Na}$  source in position number three, which  
 404 corresponds to the geometrical center of the experimental setup. A nice agreement is obtained between the experimental and the  
 405 MC simulations for both x and y-axis projections, thus validating the intrinsic PSD position-resolution obtained in the previous  
 406 work<sup>19</sup>. Finally, panel (c) shows the results for the sample-holder position number two, where the situation is comparable to the  
 407 results obtained for the fourth position.

Position	FWHM x [mm]	FWHM y [mm]
2	6.1(1)	6.2(1)
3	5.6(1)	6.1(1)
4	7.4(1)	6.9(1)

**Table 6.** Experimental x and y-axis FWHM calculated from the experimental  $^{22}\text{Na}$  PET image at the different sample positions.

408 The PET image resolution for both projection axis are calculated as the FWHM of a Gaussian fit to the experimental data.  
 409 The results are presented in Tab. 6. As expected, the best resolution in the x-axis is obtained for position number three. As one  
 410 moves away from this point, slightly broader FWHM values are obtained (positions 2 and 4) reflecting a degradation of the PET  
 411 resolution. This effect can be explained in terms of the actual intrinsic spatial resolution of the PSDs. As we move from the  
 412 geometrical center, the time-coincidences ratio between scatter and absorber planes decreases. Therefore, the resolution of the  
 413 system will be dominated by the spatial resolution of the thicker absorber detectors<sup>19</sup>.

#### 414 Compton imaging

415 The 2D Compton imaging reconstruction capability and resolution for both i-TED modules was verified by means of a short  
 416 dedicated measurement with proton beam, where the thick graphite layer was placed in the third position of the sample holder,  
 417 close to the geometrical center of the experimental setup. The incident beam energy was of 18 MeV. The 2D Compton images  
 418 independently reconstructed from the measured data for i-TED-A and i-TED-B are displayed in panels (a) and (b) of Fig. 17,  
 419 respectively. For comparison purposes, a point-like 4.4 MeV source was simulated at the same position. The MC reconstructed  
 420 images are displayed in panels (c) and (d) for i-TED-A and i-TED-B, respectively. The point-like assumption in the calculation  
 421 is justified by the fact that the Bragg peak occurs at the very end of the proton track, and therefore the majority of prompt  $\gamma$ -rays  
 422 are emitted from the same transversal plane along the x- (beam) axis.

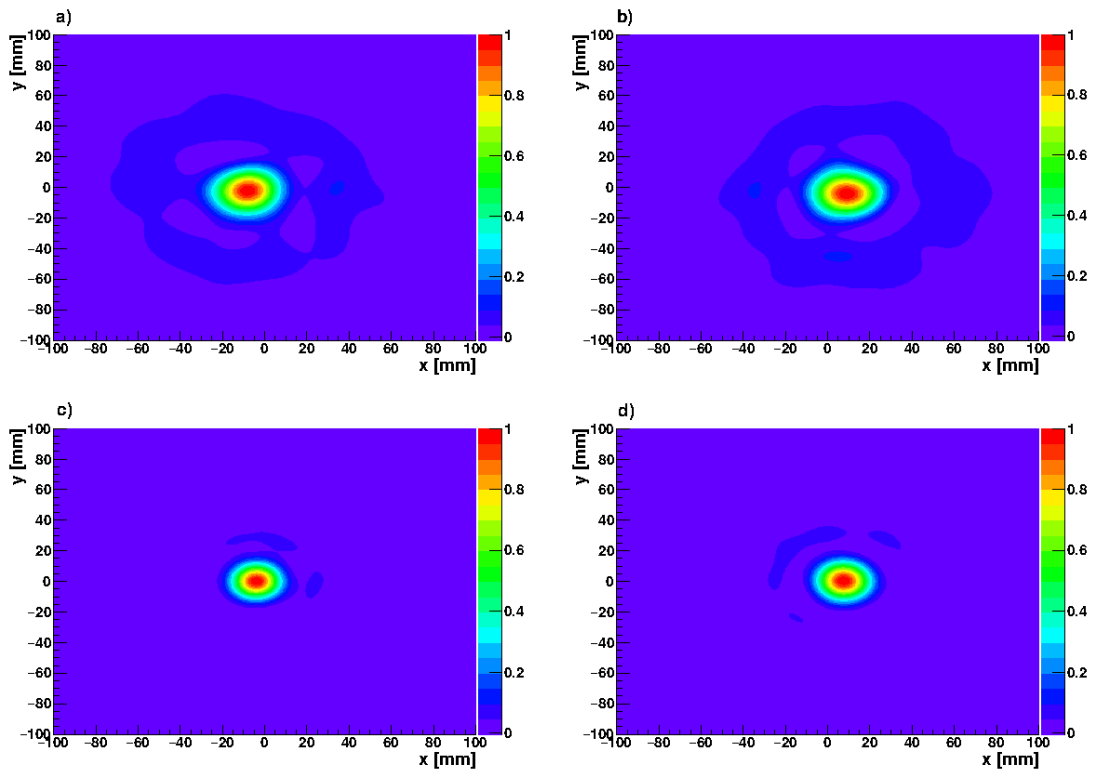


**Figure 17.** Compton images using the 4.4 MeV  $\gamma$ -ray transition from experimental data (top panels a and b) and Monte Carlo simulations (bottom panels c and d) for the thick graphite layer placed at the third slot position of the sample holder irradiated with the proton beam at CNA. See text for details.

423 A small systematic shift in the x-position was identified after a detailed comparison between the images reconstructed  
 424 in panels (a) and (b) of Fig. 17. Indeed, the position of the graphite layer is reconstructed with a difference of 10(1) mm  
 425 between i-TED-A and i-TED-B modules along the x-axis. Since the distance between the detectors was well under control, this  
 426 shift rather indicates that the central axis of both i-TED modules were not perfectly orthogonal to the beam direction (z-axis).  
 427 According to the differences in the reconstructed positions and the distance between frontal faces of i-TED modules an angle  
 428 deviation of about 2-3° with respect to the nominal 90° orientation has been estimated. No attempt has been made to correct for  
 429 such systematic bias because it does not compromise the imaging results and conclusions of the present work. On the other  
 430 hand, a more precise and reliable mechanical structure is in preparation for future similar measurements.

Detector	FWHM x [mm]	FWHM y [mm]
i-TED-A	24.73(5)	25.12(3)
i-TED-A (MC)	18.3	18.0
i-TED-B	24.26(6)	24.73(4)
i-TED-B (MC)	19.6	19.4

**Table 7.** Experimental and Monte Carlo FWHM calculated from the Compton images reconstructed using the thick graphite layer in the third position of the samples holder.

431 The FWHM values obtained for both x- and y-axis projections of the reconstructed Compton images (Fig. 17) are reported  
 432 in Tab. 7. As expected, the experimental resolutions obtained for both i-TED modules are rather comparable. Compared to  
 433 the MC point-like  $\gamma$ -ray source simulations, the resolutions obtained experimentally are broad. This might be related to other  
 434 systematic uncertainties not accounted as the real PG ray emission distribution, etc.

## 435 References

- 436 1. Knopf, A.-C. & Lomax, A. In vivo proton range verification: a review. *Phys. Medicine Biol.* **58**, DOI: [10.1088/0031-9155/58/15/r131](https://doi.org/10.1088/0031-9155/58/15/r131) (2013). <https://doi.org/10.1088/0031-9155/58/15/r131>.
- 437 2. Durante, M. & Paganetti, H. Nuclear physics in particle therapy: a review. *Reports on Prog. Phys.* **79**, 096702, DOI: [10.1088/0034-4885/79/9/096702](https://doi.org/10.1088/0034-4885/79/9/096702) (2016).
- 438 3. Durante, M., Orecchia, R. & Loeffler, J. S. Charged-particle therapy in cancer: clinical uses and future perspectives. *Nat. Rev. Clin. Oncol.* **14**, 483–495, DOI: [10.1038/nrclinonc.2017.30](https://doi.org/10.1038/nrclinonc.2017.30) (2017).
- 439 4. Durante, M. Proton beam therapy in europe: more centres need more research. *Br. J. Cancer* **120**, 777–778, DOI: [10.1038/s41416-018-0329-x](https://doi.org/10.1038/s41416-018-0329-x) (2019).
- 440 5. Krimmer, J., Dauvergne, D., Létang, J. & Testa, Prompt-gamma monitoring in hadrontherapy: A review. *Nucl. Instruments Methods Phys. Res. Sect. A: Accel. Spectrometers, Detect. Assoc. Equip.* **878**, 58–73, DOI: <https://doi.org/10.1016/j.nima.2017.07.063> (2018). Radiation Imaging Techniques and Applications.
- 441 6. Verburg, J. M. & Seco, J. Proton range verification through prompt gamma-ray spectroscopy. *Phys. Medicine Biol.* **59**, 7089–7106, DOI: [10.1088/0031-9155/59/23/7089](https://doi.org/10.1088/0031-9155/59/23/7089) (2014).
- 442 7. Parodi, K. & Polf, J. C. In vivo range verification in particle therapy. *Med. Phys.* **45**, e1036–e1050, DOI: <https://doi.org/10.1002/mp.12960> (2018). <https://aapm.onlinelibrary.wiley.com/doi/pdf/10.1002/mp.12960>.
- 443 8. Enghardt, W. *et al.* Charged hadron tumour therapy monitoring by means of pet. *Nucl. Instruments Methods Phys. Res. Sect. A: Accel. Spectrometers, Detect. Assoc. Equip.* **525**, 284–288, DOI: <https://doi.org/10.1016/j.nima.2004.03.128> (2004). Proceedings of the International Conference on Imaging Techniques in Subatomic Physics, Astrophysics, Medicine, Biology and Industry.
- 444 9. Lopes, P. C. *et al.* First in situ TOF-PET study using digital photon counters for proton range verification. *Phys. Medicine Biol.* **61**, 6203–6230, DOI: [10.1088/0031-9155/61/16/6203](https://doi.org/10.1088/0031-9155/61/16/6203) (2016).
- 445 10. Buitenhuis, H. J. T., Diblen, F., Brzezinski, K. W., Brandenburg, S. & Dendooven, P. Beam-on imaging of short-lived positron emitters during proton therapy. *Phys. Medicine Biol.* **62**, 4654–4672, DOI: [10.1088/1361-6560/aa6b8c](https://doi.org/10.1088/1361-6560/aa6b8c) (2017).
- 446 11. Tashima, H. *et al.* A single-ring OpenPET enabling PET imaging during radiotherapy. *Phys. Medicine Biol.* **57**, 4705–4718, DOI: [10.1088/0031-9155/57/14/4705](https://doi.org/10.1088/0031-9155/57/14/4705) (2012).
- 447 12. Tashima, H. *et al.* Development of a small single-ring OpenPET prototype with a novel transformable architecture. *Phys. Medicine Biol.* **61**, 1795–1809, DOI: [10.1088/0031-9155/61/4/1795](https://doi.org/10.1088/0031-9155/61/4/1795) (2016).

- 463 **13.** Tashima, H. *et al.* 3d compton image reconstruction method for whole gamma imaging. *Phys. Medicine & Biol.* **65**,  
464 225038, DOI: [10.1088/1361-6560/abb92e](https://doi.org/10.1088/1361-6560/abb92e) (2020).
- 465 **14.** Yoshida, E. *et al.* Whole gamma imaging: a new concept of PET combined with compton imaging. *Phys. Medicine & Biol.*  
466 **65**, 125013, DOI: [10.1088/1361-6560/ab8e89](https://doi.org/10.1088/1361-6560/ab8e89) (2020).
- 467 **15.** Babiano, V. *et al.* First i-TED demonstrator: A Compton imager with Dynamic Electronic Collimation. *Nucl. Instruments*  
468 *Methods Phys. Res. Sect. A: Accel. Spectrometers, Detect. Assoc. Equip.* **953**, 163228, DOI: [https://doi.org/10.1016/j.nima.](https://doi.org/10.1016/j.nima.2019.163228)  
469 [2019.163228](https://doi.org/10.1016/j.nima.2019.163228) (2020).
- 470 **16.** Domingo-Pardo, C. i-TED: A novel concept for high-sensitivity (n, $\gamma$ ) cross-section measurements. *Nucl. Instruments*  
471 *Methods Phys. Res. Sect. A: Accel. Spectrometers, Detect. Assoc. Equip.* **825**, 78 – 86, DOI: [https://doi.org/10.1016/j.nima.](https://doi.org/10.1016/j.nima.2016.04.002)  
472 [2016.04.002](https://doi.org/10.1016/j.nima.2016.04.002) (2016).
- 473 **17.** Pardo, C. D. High-sensitivity Measurements of key stellar Nucleo-Synthesis reactions. <https://hymnserc.ific.uv.es/> (2016).  
474 [Online; accessed 13-January-2021].
- 475 **18.** Lerendegui-Marco, J., Balibrea-Correa, J., Babiano-Suárez, V., Ladarescu, I. & Domingo-Pardo, C. Towards machine  
476 learning aided real-time range imaging in proton therapy (2022). [2201.13269](https://doi.org/10.2201/13269).
- 477 **19.** Balibrea-Correa, J. *et al.* Machine learning aided 3d-position reconstruction in large  $\text{LaCl}_3$  crystals. *Nucl. Instruments*  
478 *Methods Phys. Res. Sect. A: Accel. Spectrometers, Detect. Assoc. Equip.* **1001**, 165249, DOI: [https://doi.org/10.1016/j.](https://doi.org/10.1016/j.nima.2021.165249)  
479 [nima.2021.165249](https://doi.org/10.1016/j.nima.2021.165249) (2021).
- 480 **20.** Universidad de Sevilla, C. Centro nacional de aceleradores. <http://cna.us.es/index.php/es/> (2020).
- 481 **21.** Baratto-Roldán, A. *et al.* Preparation of a radiobiology beam line at the 18 mev proton cyclotron facility at cna. *Phys.*  
482 *Medica* **74**, 19–29, DOI: <https://doi.org/10.1016/j.ejmp.2020.04.022> (2020).
- 483 **22.** Baratto-Roldán, A. *et al.* Feasibility study of a proton irradiation facility for radiobiological measurements at an 18 mev  
484 cyclotron. *Instruments* **2**, DOI: [10.3390/instruments2040026](https://doi.org/10.3390/instruments2040026) (2018).
- 485 **23.** Rodríguez-González, T. *et al.* Production yields of emitters for range verification in proton therapy. *EPJ Web Conf.* **239**,  
486 24003, DOI: [10.1051/epjconf/202023924003](https://doi.org/10.1051/epjconf/202023924003) (2020).
- 487 **24.** Rodríguez-González, T. *et al.* Production yields at the distal fall-off of the  $\alpha$  emitters  $^{11}\text{C}$  and  $^{13}\text{N}$  for in-vivo range  
488 verification in proton therapy. *Radiat. Phys. Chem.* **190**, DOI: [10.1016/j.radphyschem.2021.109759](https://doi.org/10.1016/j.radphyschem.2021.109759) (2022).
- 489 **25.** Di Francesco, A. *et al.* TOFPET 2: A high-performance circuit for PET time-of-flight. *Nucl. Instruments Methods Phys.*  
490 *Res. Sect. A: Accel. Spectrometers, Detect. Assoc. Equip.* **824**, 194 – 195, DOI: <https://doi.org/10.1016/j.nima.2015.11.036>  
491 (2016). Frontier Detectors for Frontier Physics: Proceedings of the 13th Pisa Meeting on Advanced Detectors.
- 492 **26.** Yap, J., De Franco, A. & Sheehy, S. Future developments in charged particle therapy: Improving beam delivery for  
493 efficiency and efficacy. *Front. Oncol.* **11**, DOI: [10.3389/fonc.2021.780025](https://doi.org/10.3389/fonc.2021.780025) (2021).
- 494 **27.** Jolly, S., Owen, H., Schippers, M. & Welsch, C. Technical challenges for flash proton therapy. *Phys. Medica* **78**, 71–82,  
495 DOI: <https://doi.org/10.1016/j.ejmp.2020.08.005> (2020).
- 496 **28.** Tomitani, T. & Hirasawa, M. Image reconstruction from limited angle Compton camera data. *Phys. Medicine Biol.* **47**,  
497 2129–2145, DOI: [10.1088/0031-9155/47/12/309](https://doi.org/10.1088/0031-9155/47/12/309) (2002).
- 498 **29.** Klein, O. & Nishina, Y. Über die Streuung von Strahlung durch freie Elektronen nach der neuen relativistischen  
499 Quantendynamik von Dirac. *Zeitschrift für Physik* **52**, 853–868, DOI: [10.1007/BF01366453](https://doi.org/10.1007/BF01366453) (1929).
- 500 **30.** Nickolls, J., Buck, I., Garland, M. & Skadron, K. Scalable Parallel Programming with CUDA. *Queue* **6**, 40–53, DOI:  
501 [10.1145/1365490.1365500](https://doi.org/10.1145/1365490.1365500) (2008).
- 502 **31.** Allison, J. *et al.* Recent developments in Geant4. *Nucl. Instruments Methods Phys. Res. Sect. A: Accel. Spectrometers,*  
503 *Detect. Assoc. Equip.* **835**, 186 – 225, DOI: <https://doi.org/10.1016/j.nima.2016.06.125> (2016).
- 504 **32.** Verburg, J. M., Shih, H. A. & Seco, J. Simulation of prompt gamma-ray emission during proton radiotherapy. *Phys.*  
505 *Medicine Biol.* **57**, 5459–5472, DOI: [10.1088/0031-9155/57/17/5459](https://doi.org/10.1088/0031-9155/57/17/5459) (2012).
- 506 **33.** Olleros, P. *et al.* On the performance of large monolithic  $\text{LaCl}_3(\text{Ce})$  crystals coupled to pixelated silicon photosensors. *J.*  
507 *Instrumentation* **13**, P03014–P03014, DOI: [10.1088/1748-0221/13/03/p03014](https://doi.org/10.1088/1748-0221/13/03/p03014) (2018).

## 508 **Acknowledgements**

509 This work has been carried out in the framework of a project funded by the European Research Council (ERC) under the  
510 European Union's Horizon 2020 research and innovation programme (ERC Consolidator Grant project HYMNS, with grant  
511 agreement No. 681740). The authors acknowledge support from the Spanish Ministerio de Ciencia e Innovación under grants  
512 PID2019-104714GB-C21, FPA2017-83946-C2-1-P, FIS2015-71688-ERC, FPA2016-77689-C2-1-R, RTI2018-098117-B-C21,  
513 CSIC for funding PIE-201750I26 and from the European H2020-847552 (SANDA). This work was partially supported by  
514 Generalitat Valenciana PROMETEO/2019/007. T. Rodriguez-Gonzalez acknowledges the Spanish FPI predoctoral grant. We  
515 would like to thank the crew at the Electronics Laboratory of IFIC, in particular Manuel Lopez Redondo and Jorge Nácher  
516 Arándiga for their excellent and efficient work.

## 517 **Author contributions statement**

518 **J.B.C:** Investigation, Methodology, Formal analysis, Software, Data curation, Writing - original draft. **J.L.M:** Investigation,  
519 Methodology, Formal analysis, Data curation, Visualization, Writing - review draft. **I.L:** Software, Visualization. **C.D.P:**  
520 Conceptualization, Methodology, Investigation, Supervision, Writing - original draft & editing, Funding acquisition. **C.G:** In-  
521 vestigation, Methodology. **T.R.G:** Investigation, Formal analysis. **M.C.J.R:** Investigation, Methodology. **B.F.M:** Investigation.

## 522 **Additional information**

523 **Competing interests:** The authors declare that they have no known competing financial interests or personal relationships that  
524 could have appeared to influence the work reported in this paper.